Tumor ablation due to inhomogeneous anisotropic diffusion in generic three-dimensional topologies

Erdi Kara
Department of Mathematics and Statistics, Texas Tech University, Lubbock TX

Aminur Rahman*
Department of Applied Mathematics, University of Washington, Seattle WA

Eugenio Aulisa
Department of Mathematics and Statistics, Texas Tech University, Lubbock TX

Souparno Ghosh
Department of Statistics, University of Nebraska - Lincoln, Lincoln NB

(Received 6 January 2020; revised 28 May 2020; accepted 23 November 2020; published 30 December 2020)

In recent decades computer-aided technologies have become prevalent in medicine, however, cancer drugs are often only tested on *in vitro* cell lines from biopsies. We derive a full three-dimensional model of inhomogeneous -anisotropic diffusion in a tumor region coupled to a binary population model, which simulates *in vivo* scenarios faster than traditional cell-line tests. The diffusion tensors are acquired using diffusion tensor magnetic resonance imaging from a patient diagnosed with glioblastoma multiform. Then we numerically simulate the full model with finite element methods and produce drug concentration heat maps, apoptosis hotspots, and dose-response curves. Finally, predictions are made about optimal injection locations and volumes, which are presented in a form that can be employed by doctors and oncologists.

DOI: 10.1103/PhysRevE.102.062425

I. INTRODUCTION

There is an ongoing struggle in cancer treatments to develop therapies that kill a majority of tumor cells, while having negligible effect on healthy cells. Treatments for brain tumors are especially delicate as brain tumors are associated with very high mortality. The five-year survival rate for people with a malignant brain or central nervous system tumor is approximately 34% for men and 36% for women in the United States and brain tumors account for 85% to 90% of all primary central nervous system tumors [1].

One of the major obstacles to improve current treatments is the presence of some physical barriers such as the blood-brain barrier (BBB) and the blood-brain tumor barrier (BBTB) impeding drugs from reaching the tumor sites in the brain [2–4]. The BBB, existing between the brain's microvessels and tissue, prevents many macromolecules from entering interstitial space in the brain; thus separating the central nervous system and systemic circulation of the body. It is reported in Ref. [5] that BBB prevents entry of approximately 98% of the small molecules and nearly 100% of large molecules, such as recombinant proteins or gene-based medicines into brain tumors from the vascular compartment. Similarly, the BBTB is located between brain tumor tissues and the brain's blood vessels formed by highly specialized endothelial cells, limiting the delivery of most anticancer drugs to tumor tissue. To overcome the challenges associated with these barriers, several methods have been developed such as intrarterial administration, barrier disruption, drug packaging, and inhibiting drug efflux from tumors [6]. Regardless, oral and intravascular administration allows only a small fraction of therapeutic agents to reach the tumor region in the brain because the drug concentration decreases precipitously due to the sink effect of the extracellular space along the route of drug transport to the tumor region; thus, necessitating the administration of a high dose to achieve sufficient drug concentrations to kill the tumor cells. Unfortunately, physiological toxicity limits the amount of therapeutic agent allowed in a particular therapy.

Significant effort has gone into developing therapies with high efficacy to toxicity ratios through the use of lower drug concentrations via direct administration in targeted regions. One such method is discussed in de Boer *et al.* [5]. Drug injection therapies allow for uncomplicated individualized treatment for solid accessible tumors [5,7–10]. Further, these types of therapies provide us with an opportunity to optimize drug efficacy by changing the fluidic properties of the injection as shown by Morhard *et al.* [9]. While testing a variety of therapeutic agents on animals is time intensive and costly, numerical simulations may prove to be a cheap and effective solution.

In order to conduct numerical experiments on the effects of drugs on cancerous tumors, we need transport–population coupled models. Transport models often focus on the dynamics of therapeutic drug delivery processes to the tumor site by blood flow through capillaries and tissues. To reach the cancer cells, relevant agents must enter the tumor interstitial fluid through the blood vessels walls of the tumor [11]. Drug-transport modeling is a relatively well-established field

*arahman2@uw.edu

[12], and several models investigating various aspects of this process can be found in the literature [13–16]. As noted in Ref. [11], in order for the drug therapies to be successful, the agent must be effective on the the corresponding cancer type in the in vivo setting and an optimal amount of drugs must be delivered to the tumor site. Mathematical modeling plays a crucial role in understanding these therapies. For example, in the case of nanoparticle therapies [17–19], drug transport has been modeled extensively [20–23]. While there are many sophisticated models for drugs penetrating into tumor from the blood stream, there are few mathematical investigation of drugs injected directly into the solid tumor [24–26].

Administered drugs can lead to partial or full ablation of tumor cells as well as produce toxicity or side effects on the healthy cells [27,28]. Moreover, tumor cells can also develop resistance to the corresponding drug [29–31]. The internal dynamics of the tumor, regardless of the drug exposure, also play a crucial role in a successful cancer therapy. Thus, most of the aforementioned models above and many other studies in the literature investigate tumor growth and invasion [32–36], formation of new blood vessels in the tumor (antiogenesis) [37,38], and the ability of cancer cells to migrate to a different location (metastasis) [39,40]. For a more comprehensive presentation of cancer population dynamics literature, we refer the reader to the text of Kuang *et al.* [41].

In Ref. [42], Rahman *et al.* present a simple drug diffusion-binary population model. It is assumed that a drug is being injected directly into the center of a homogeneous-isotropic spherical tumor, and hence the diffusion is radial with constant diffusivity. Furthermore, it is assumed that a cell is either dead if the concentration of the drug is greater than a threshold and alive if the concentration is less than this threshold; i.e., the drug acts as a trigger for cell death. From this model dose-response curves (response as a function of dose) are produced in order to relate it to relevant empirical data, such as Harvard Medical School's LINCS data base [43,44]. Since the data set does not include replication studies, artificial replication dose-response curves were produced, and the dose-response curves from the mechanistic model were shown, in many cases, to lie within 95% piecewise-linear confidence bands.

While the model of Rahman *et al.* [42] performed well against artificial replication data, the simplicity is burdened by the baggage of assumptions. Transport of drugs in the brain is a complex process due to the highly inhomogeneous and anisotropic structure of brain tissue, local pressure differences, and chemcial interactions of the drug with the surrounding tissue. However, a model that does not obviate negligible contributions falls prey to computational constraints. Even with parallelization on a supercomputing cluster, would it be useful to an oncologist that is working directly with a patient?

In this investigation, we keep the simple binary population model, and explore the complexities of drug transport from a single injection into deformed globular tumors (topological 3 spheres). It is well known that diffusion dominates, but we assume it can be inhomogeneous and anisotropic. This allows for fast *in vivo* simulations of direct injection therapies, which we use to produce dose-response curves, apoptosis hotspots, and optimal injection locations. This investigation, using patient specific DTI data with a transport-population model, endeavors to present results to aid practitioners in optimizing treatment strategies.

The remainder of the paper is organized as follows: We begin our discussions by deriving the inhomogeneous-anisotropic diffusion and binary population models in Sec. II. Then in Sec. III, we develop the computational foundation of the investigation in two steps. First, Sec. III A sets up the finite element scheme. We use Galerkin finite element method for the spatial discretization and a Crank-Nicolson scheme for the temporal integration. Then the diffusion tensors are constructed from patient magnetic resonance imaging (MRI) data in Sec. III B. Section IV presents the numerical simulations and oncological predictions of our study. We first examine the drug diffusion in the tumor and observe the high inhomogeneity and anisotropy in the concentration heat maps. Then the apoptosis is simulated by invoking the binary population model. This allows us to create dose-response curves. Importantly, the model predicts optimal injection sites, evidenced by the dose-response curves, different from what intuition might suggest. Finally, the investigation is concluded in Sec. V with a discussion on viable oncological applications and future modeling directions.

II. DRUG DIFFUSION AND BINARY POPULATION MODELS

In this section we derive the inhomogenous- anisotropic diffusion model and the binary tumor population model. First we write a general diffusion model. It has been shown through MRI in the brain that tumors often grow in an inhomogeneous-anisotropic diffusionlike manner [45–48]. Using diffusion tensor imaging (DTI) techniques [49], the effective diffusivity of water in tissue can be estimated. Since there is a large contrast between cancerous and healthy tissues, DTI can be used to map the geometry of a tumor and estimate the diffusivity of water in a tumor [50–52]. Finally, it is worth noting, due to the infiltrative nature of gliomas, when we use the word "tumor" we are referring to a tumor region in a similar fashion to the seminal works of Scherer [53].

Consider a drug with molarity u diffusing from an injection into a porous tumor, with an effective diffusivity tensor $\mathbf{D}$. Next for the sake of brevity, let $\mathbf{x} = (x_1, x_2, x_3)$ be the position vector. Finally, we model the leak at the boundary of the region of interest as "Newton's law of cooling" [54]. This gives us the generic model in Cartesian coordinates

$$\frac{\partial u(\mathbf{x};t)}{\partial t} = \nabla \cdot (\mathbf{D}(\mathbf{x})\nabla u(\mathbf{x};t)), \quad \mathbf{x} \in \Omega; \tag{1a}$$

$$\mathbf{D}(\mathbf{x})\nabla u(\mathbf{x};t) \cdot n = -\gamma u(\mathbf{x};t), \quad \mathbf{x} \in \partial\Omega; \tag{1b}$$

$$u(\mathbf{x};t=0) = \bar{u}(\mathbf{x}), \tag{1c}$$

where $\bar{u}(\mathbf{x})$ is some generic initial concentration profile of the drug soon after injection and γ is the constant leak coefficient. We treat the boundary as a buffer zone containing only noncancerous cells such that the rate of leakage is similar to the rate of diffusion at the boundary. Moreover, we neglect the chemical reactions, absorption, and adsorption of the drug following a similar approach presented in Ref. [24].

We now impose a specific initial condition. In Ref. [42] a bump function (compact Gaussian) decaying to zero just

within the domain was used. This represents the short timescale spread of the distribution profile from an initial Dirac delta function. During inhomogeneous-anisotropic diffusion, the drug does not diffuse evenly, and hence a bump function that extends to the endpoints would not capture the irregularities expected in such a problem. Nevertheless, there are many numerical advantageous to using a bump function. We may either introduce a sharper bump or try to capture the diffusive irregularities in the initial condition. In general, for an injection at point $\mathbf{x}_c$, we have

$$\bar{u}(r) = \frac{U_0}{V_b}\begin{cases}\exp\left(1 - \frac{R_b^2}{R_b^2 - r^2}\right), & r < R_b \\ 0, & r \geqslant R_b,\end{cases} \tag{2}$$

where, $r = \|\mathbf{x} - \mathbf{x_c}\|$, R_b is the radius of the bump, U_0 is the injected concentration, and V_b is the normalization constant for the bump function; that is,

$$V_\mathrm{b} = \int_0^{\pi}\int_0^{2\pi}\int_0^{R_\mathrm{b}} \exp\left(1 - \frac{R_\mathrm{b}^2}{R_\mathrm{b}^2 - r^2}\right) r^2 \sin\phi \, dr d\theta d\phi.$$

A. Binary population model

As done in Ref. [42], we use a binary population model: the tumor cell is dead after some exposure time τ (which is much larger than the diffusive time scale), if at any time during the diffusion process the drug concentration is above some given threshold value $u_T(\tau)$, otherwise it is alive. Suppose that the rate of cell death is equivalent to the rate of cell growth; thereby negating external factors such as nutrition and programed cell death. This allows us to focus on cell death due to the drug concentration, which we expect to be the major contributing factor, unless the drug is ineffective. We expect the threshold to decrease with time because it takes more toxins to kill a cell quickly than it does to kill it slowly. Further, since dose response to drugs is often assumed to be sigmoidal [41], we expect u_T to be a negative exponential with time τ,

$$u_T(\tau) = a - be^{-c\tau}, \tag{3}$$

where the parameters a, b, and c are back calculated from a representative sample of the Harvard Medical School LINCS drug data base [43,44]. From the representative sample we calculate what $u_T(\tau = 24\ \text{hrs})$, $u_T(\tau = 48\ \text{hrs})$, $u_T(\tau = 72\ \text{hrs})$ must be in order to produce the empirically observed response. It should be noted that u_T may not be monotonic based on drug resistance and other biological effects.

We have three equations with three unknowns, which is solved explicitly in Ref. [42]. In this paper, we use the following representative threshold values calculated from the dose-response data of cell-line "C32" and drug "Selumetinib" from the LINCS data set:

$$u_T(24) = 0.230153\ \mu\text{M},$$
$$u_T(48) = 0.0700055\ \mu\text{M},$$
$$u_T(72) = 0.0499662\ \mu\text{M}.$$

From these threshold values, we calculate the parameters of (3),

$$a \approx 0.0471, \quad b = -1.4629, \quad \text{and} \quad c = 0.0866.$$

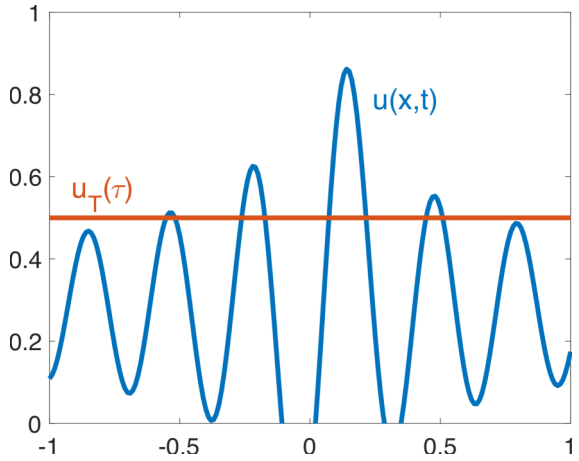

FIG. 1. A 1D example of the binary population model. Whenever $u(\mathbf{x}, t) > u_T(\tau)$, the cells in position $\mathbf{x}$ contribute to the apoptosis fraction.

A simple one-dimensional (1D) example of how the binary population works in practice is illustrated in Fig. 1. From the figure whenever $u(\mathbf{x}, t) > u_T(\tau)$ we calculate the fraction of tumor cells killed due to the exposure at diffusion time, t. If the concentration at point $\mathbf{x}$ is ever greater than the threshold, that point contributes to the apoptosis fraction. Then we integrate all the apoptosis points over diffusion time $t \in [0, T]$ and divide by the length of the entire interval $[-1, 1]$.

III. NUMERICAL PROCEDURE

In this section, we first describe the numerical procedure to approximate the solution of the system (1) in Sec. II. Galerkin finite element method (GFEM) is used for the spatial discretization and a Crank-Nicolson scheme for the temporal integration. For a practical introduction finite element method, the reader can refer to Ref. [55].

For the inhomogeneous-anisotropic diffusivity we incorporate diffusion tensors from DTI data. The magnetic field gradients in different directions from the MRI is used to map out directions of faster and slower diffusion that is normalized to the diffusivity of water molecules. While in medical imaging the diffusion tensor is predominantly used to identify anomalies, and often averaged out in preferential directions for that reason, we use the tensor itself in the diffusivity of the transport model. Thus allowing us to produce accurate qualitative simulations of *in vivo* scenarios.

There are a few studies in the literature integrating FEM with DTI in a modeling framework. Kraft *et al.* incorporated DTI with FEM to investigate the mechanics of neurotrauma [56]. In Ref. [57], Ramasamy *et al.* proposed a subject-specific finite element model for the residual limb to assess the effect of a particular socket on deep tissue injury. They utilized DTI to reveal the anatomy of muscle fiber and mapped the information onto a finite element mesh. A nonlinear hyperelastic, transversely isotropic skeletal muscle constitutive law containing a deep tissue injury model were then solved with FEM. Clatz *et al.* [58] used FEM to simulate the invasion of GBM in the brain parenchyma and its mass effect on the invaded tissue. They described a coupling strategy between

reaction-diffusion and linear elastic mechanical constitutive equations where diffusion tensor information was provided by DTI. In Ref. [24], a convection-enhanced drug delivery (CED), where the anticancer agent is directly administered into the brain tissue, was introduced. Governing equations concerning the transport of the therapeutic agent and tissue deformation was solved with the finite volume method, where the information about the structures of the tissue is acquired through DTI.

A. Finite element discretization

Consider the Sobolev space $H^1(\Omega) = \{v \in L^2(\Omega) : \partial_{x_i} v \in L^2(\Omega) \quad i = 1, 2, 3\}$, where Ω is the domain of the PDE from Sec. II. If u is sufficiently smooth, by multiplying Eq. (1a) with a test function $v \in H^1(\Omega)$ and integrating over Ω using a Green's formula, we obtain the variational formulation of (1a); that is, find u such that for every $t \in I = [0, T]$,

$$\int_\Omega \frac{\partial u}{\partial t} v dx = -\int_\Omega \mathbf{D}\nabla u \cdot \nabla v dx - \int_{\partial\Omega} \gamma u v ds, \quad \forall v \in H^1(\Omega), \quad t \in I. \tag{4}$$

Let

$$\Omega_h = \{K_1, K_2, .., K_n\} \tag{5}$$

be a geometrically conforming hexagonal triangulation of Ω.

As a test space, we use the space of scalar valued piecewise quadratic polynomials; i.e.,

$$V_h = \{p \in C^0(\bar{\Omega}) \ : \ p|_K \in Q_2(K), \forall K \in \Omega_h\} \subset H^1(\Omega).$$

Replacing $H^1(\Omega)$ with V_h, the finite element formulation of Eq. (4) reads: find u_h such that for every $t \in I$,

$$\int_\Omega \frac{\partial u_h}{\partial t} v_h dx = -\int_\Omega \mathbf{D}\nabla u_h \cdot \nabla v_h dx - \int_{\partial\Omega} \gamma u_h v_h ds, \quad \forall v_h \in V_h, \quad t \in I. \tag{6}$$

Let $\{\psi_i\}_{i=1}^n$ be a basis of the space V_h consisting of the orthogonal nodal basis functions satisfying $\psi_i(N_j) = \delta_{ij}$ for every nodal point N_j. For every $u_h \in V_h$, there exist time dependent coefficients $\xi_j(t)$ such that

$$u_h(x, t) = \sum_{j=1}^{n} \xi_j(t)\psi_j(x). \tag{7}$$

From this construction, $\xi_j(t)$'s are the nodal values of u_h for every time t. If we substitute Eq. (7) in Eq, (6), we obtain the following system of ordinary differential equations:

$$M\dot{\xi}(t) = -(A + R)\xi(t), \tag{8}$$

where $\xi(t) = [\xi_1(t), \xi_2(t), .., \xi_n(t)]^T$ and

$$M_{ij} = \int_\Omega \psi_j \psi_i, \quad A_{ij} = \int_\Omega \mathbf{D}\nabla\psi_j \cdot \nabla\psi_i, \quad R_{ij} = \int_{\partial\Omega} \gamma \psi_j \psi_i. \tag{9}$$

Note that the diffusion tensor $\mathbf{D}$ is defined element wise. Let $0 = t_0 < t_1 < \ldots < t_N = T$ be a partition of the interval $[0, T]$ with the constant time step $\Delta t = t_{n+1} - t_n$. Application of the Crank-Nicolson scheme for Eq. (8) yields

$$M\frac{\xi_{k+1} - \xi_k}{\Delta t} = -(A + R)\frac{\xi_k + \xi_{k+1}}{2}, \tag{10}$$

where ξ_0 is chosen as the nodal values of $\bar{u}(x)$ defined in Eq. (1c) of Sec. II. For the remainder of the manuscript we take the step size $\Delta t = 0.02$ with $N = 60$ equal time intervals and the leak coefficient is set to $\gamma = 0.002$. For the implementation of the problem (10), we use the open source finite element C++ library FeMUS [59].

B. Incorporating the diffusion tensor

Diffusion patterns of water molecules in biological tissue can be visualized by means of DTI. The diffusivity in the medium is quantified at each image voxel (a volumetric pixel) with a diffusion tensor that relates diffusive flux to a concentration gradient in each Cartesian direction. The three diagonal elements D_{xx}, D_{yy}, and D_{zz} represent diffusion coefficients measured along each of the principal x, y, and z axes. The six off-diagonal entries quantify the correlation of Brownian motion between corresponding principal directions. A generic diffusion tensor can be written as

$$\mathbf{D} = \begin{bmatrix} D_{xx} & D_{xy} & D_{xz} \\ D_{yx} & D_{yy} & D_{yz} \\ D_{zx} & D_{zy} & D_{zz} \end{bmatrix}, \tag{11}$$

where D_{ij} has the unit of mm^2/s.

The diffusivities from DTI are usually averaged out and illustrated by condensing the tensor information into a scalar quantity or plotted as a color encoded texture map. The former consists of scalar measurements to quantify the magnitude or the shape of the diffusion. In terms of magnitude, mean diffusivity, which is the mean of the eigenvalues of the diffusion tensor, is one of the most common scalar measurements. On the other hand, fractional anisotropy, which is the normalized variance of the eigenvalues, is the most commonly used anisotropy measure. In addition to various scalar measurements, one can also consider the direction of the major eigenvector (the eigenvector associated with the largest eigenvalue) and create a color map for the corresponding directions. The most commonly used color scheme in terms of anatomical planes is as follows; blue is superior-inferior, red is left-right, and green is anterior-posterior [49]. For an extensive overview of the diffusion tensor imaging, the reader may refer to Ref. [60].

To capture the anisotropies of the diffusion in our numerical simulations we use a dataset that includes a diffusion tensor magnetic resonance image of a 35-year old male diagnosed with glioblastoma multiform (GBM). The dataset can be found in the tutorial [61]. From the diffusivity data, in Fig. 2, we derive and display the major eigenvector direction (indicated by the colors prescribed in the preceding paragraph), fractional anisotropy, and mean diffusivity. In the figure the GBM region can be observed around the right frontal lobe.

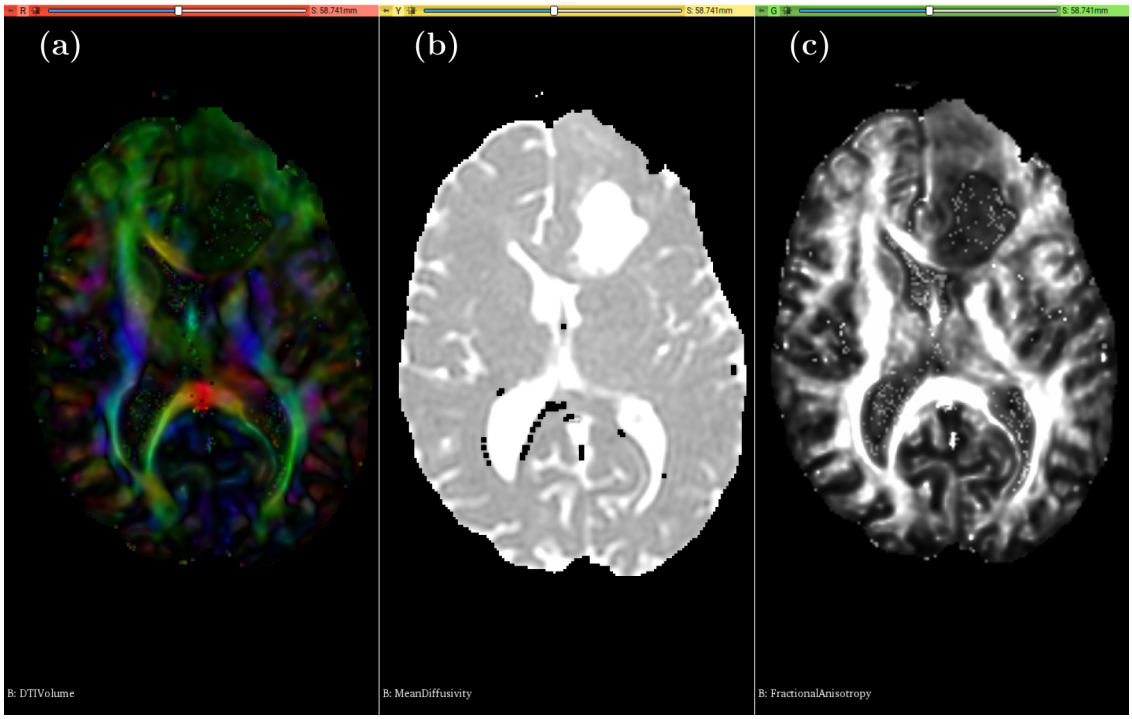

FIG. 2. Axial view of the brain DTI with illustrations from *3DSlicer* of (a) the major eigenvalue direction, (b) fractional anisotropy, and (c) mean diffusivity. In all images the tumor region can be seen around the right frontal lobe.

The coordinate dimensions of the sample volume is $256 \times 256 \times 51$ with voxel size $1 \times 1 \times 2.6$ mm. In the preprocessing of the DTI volume, we utilized the open source software *3DSlicer* [62], which allows advanced medical image analysis and processing. It provides a graphical user interface with various modules as well as a Python console, which gives access to data arrays of image models for further analysis.

The diffusion tensor is symmetric and positive definite but in practice the positive definiteness can be corrupted due to measurement noise. Thus we first resample the DTI volume to correct the tensors that are not positive semidefinite. We are particularly interested in diffusion in the tumor tissue. Hence, we extract a region of $64 \times 64 \times 64\,\text{mm}^3$ from the resampled volume enclosing the entire tumor region and centered at the origin to create the region,

$$\Omega = \{(x, y, z) : -32\,\text{mm} \leqslant x, y, z \leqslant 32\,\text{mm}\}. \tag{12}$$

We take Ω as the computational domain of the problem described in Eq. (1). After the rescaling, the tumor region fits completely inside the rectangular subdomain of Ω,

$$\begin{aligned}\mathbb{T} = \{(x, y, z) : &-7.68\,\text{mm} \leqslant x \leqslant 21.76\,\text{mm},\\ &-19.2\,\text{mm} \leqslant y \leqslant 19.2\,\text{mm},\\ &-14.08\,\text{mm} \leqslant z \leqslant 28.16\,\text{mm}\} \subset \Omega.\end{aligned} \tag{13}$$

Now let

$$\mathbf{D}_i = \begin{bmatrix} D_{xx} & D_{xy} & D_{xz} \\ D_{yx} & D_{yy} & D_{yz} \\ D_{zx} & D_{zy} & D_{zz} \end{bmatrix} \tag{14}$$

be the diffusion tensor defined for the hexagonal element K_i in Eq. (5). Note that we define $\mathbf{D}$ element wise so it is essentially piece-wise discontinuous across the problem domain. Let $\mathbf{D}_i^a = (D_{xx} + D_{yy} + D_{zz})/3$ be the element-wise apparent diffusion coefficient (ADC).

A major prediction made in this investigation is the fraction of the tumor volume killed against preassigned thresholds, $u_T(24)$, $u_T(48)$, and $u_T(72)$, from Sec. II A. This task essentially requires the elementwise identification of the tumor cells in Ω. The only quantitative information about the sample data are the diffusion tensors at each voxel provided by DTI. No method is known to precisely differentiate the tumor and healthy cells by means of diffusion tensor information. However, we employ the fact that water diffuses significantly faster in GBM tissue than the surrounding healthy tissue [63].

We first assume that there is no tumor cell outside the region $\mathbb{T}$. Then, we will mark any element K_i in $\mathbb{T}$ as cancerous if $\mathbf{D}_i^a > 0.002$. This is the value where we observe a relatively sharp transition between the normal and cancerous regions. To calculate the apoptosis fraction, first consider the unit step function

$$H(s) = \begin{cases} 1, & s > 0, \\ 0, & s \leqslant 0; \end{cases} \tag{15}$$

and the subregion $\mathbb{T}_C \subset \mathbb{T}$ defined as

$$\mathbb{T}_C = \left\{\mathbf{x} \in \mathbb{T} : \mathbf{D}_i^a(\mathbf{x}) > 0.002\right\}. \tag{16}$$

We compute the fraction of cells, $\beth$, that were once exposed to a concentration higher than u_T at the simulation time $t = t_n$ as follows:

$$\beth(\tau, t_n) = \frac{\int_{\mathbb{T}_C} H\left(\max_{t\in[0,t_n]}[u(\mathbf{x}, t) - u_T(\tau)]\right) dV}{\int_{\mathbb{T}_C} dV}, \tag{17}$$

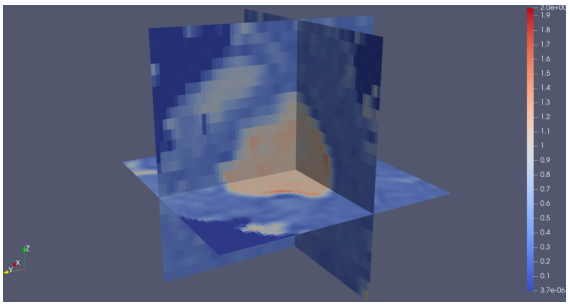

FIG. 3. Computational domain with three representative slices centered at $\mathbf{x}_c = (6.4\,\text{mm}, 0, 0)$. The heat map indicates the magnitude of the ADC. The color scheme is scaled to a visibly distinguishable range.

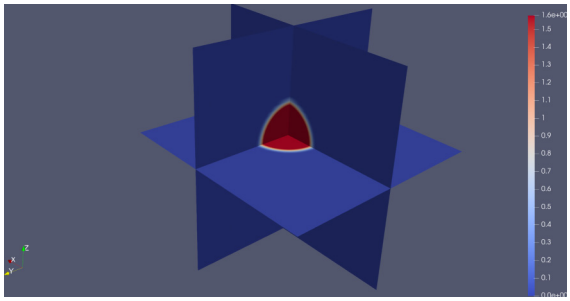

FIG. 4. Initial concentration profile $u(\mathbf{x}; t = 0\,\text{s})$ centered at the location $\mathbf{x}_c = (6.4\,\text{mm}, 0, 0)$ with an initial injection molarity of $U_0 = 1.5\ \mu\text{M}$.

where $\tau = 24,\ 48$, or 72 h. Then to get the apoptosis fraction, $\aleph$, we prescribe $t_n = T$ in Eq. (17),

$$\aleph(\tau) = \beth(\tau, T). \tag{18}$$

Note that the resulting fractions above are relative to the subregion $\mathbb{T}_C$ since we assume all tumor cells lie in $\mathbb{T}_C$.

Different cross sections of the computational domain Ω indicating the element-wise ADCs can be seen in Fig. 3. We construct Ω to be consistent with the anatomical coordinate system described in Ref. [64]. Positive directions of the x, y, and z axes are chosen to be anterior, left, and superior, respectively. Consequently, xy, xz, and yz coordinate planes correspond to transverse, sagital, and frontal planes, respectively. In Fig. 3, for example, the horizontal plane with respect to the monitor corresponds to the transverse plane.

DTI is a noninvasive technique based on the measurement of the diffusion of water molecules. Therefore, the diffusion tensor $\mathbf{D}$ may be quantitatively different across the tissue of interest when another substance, such as a therapeutic agent, is used. Seemingly, there is no experimental study proposing a numerical relationship between the diffusion tensor of water and other fluids in brain tissue. Therefore, we will assume that although water and corresponding drug molecules have different fluidic properties, they display qualitatively similar behavior in the same medium. With this assumption, we will treat the diffusion tensors that we extracted from the dataset, described above, as the diffusion tensors of the agent used in the simulated treatment. For information on treatments of this type, the reader can refer to [24,58].

IV. RESULTS AND PREDICTIONS

In this section we present the *in vivo* direct injection treatment simulations resulting from the numerical solutions of our model (1). Based on the location of $\mathbb{T}$, we set the initial condition (15) (illustrated in Fig. 4) as follows:

$$u(\mathbf{x}; t = 0) = \frac{U_0}{V_b} \begin{cases} \exp\left(1 - \frac{R_b^2}{R_b^2 - r^2}\right) & \text{for } r \leqslant R_b, \\ 0 & \text{for } r \geqslant R_b; \end{cases} \tag{19}$$

where $V_b = 1.1990\,\text{mm}^3$, $R_b = 12.8\,\text{mm}$, and $r = \sqrt{(x - 6.4)^2 + y^2 + z^2}$. We set a very high initial concentration of $U_0 = 1.5\ \mu\text{M}$ for illustrative purposes.

In Sec II A, we assumed that if the concentration at the element K_i is above a certain threshold, $u_T(\tau)$, at any simulation time, t, then K_i will die out after the corresponding exposure times, τ. With this assumption, we can create a heat map indicating the regions, which is predicted to die after the related exposure times, $\tau = 24$, 48, and 72 h. It should be noted that although the precise tumor region is $\mathbb{T}_C$, we will display the apoptotic region within $\mathbb{T}$ for illustration purposes. Also note that the drugs eventually leak out beyond the region $\mathbb{T}_C$ and can reach unintended regions of the brain resulting in unpredictable side effects. In several clinical brain tumor trials, poor targeting of the tumor region is identified as one of the most significant obstacles to efficient implementation of CED [65,66]. Thus, the spread of the drug into the healthy brain tissue can be considered as one of the potential sources of toxicity which may arise in CED therapies. Other sources of toxicity may be from the physical damage to the brain tissue caused by the catheter, mechanical stress induced by the infusion of the drug, or the type of drug used [67–71]. In this work, we assume that any cell exposed to concentrations above the threshold, $u_T(\tau)$, will have an adverse reaction to the drug, and we leave a more detailed investigation of toxicity to a future study.

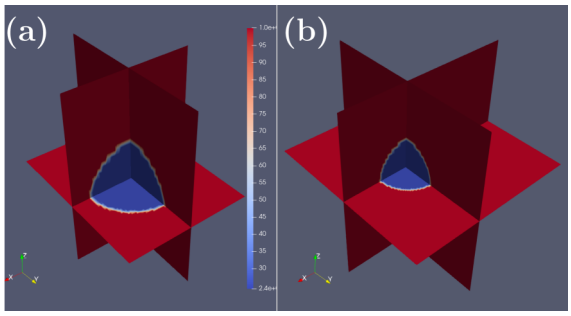

FIG. 5. Apoptotic region induced by the initial bump function centered at $\mathbf{x}_c = (6.4\,\text{mm}, 0, 0)$, with a very high drug concentration of $U_0 = 1.5\ \mu\text{M}$ for illustration purposes, within (a) the tumor region $\mathbb{T}$ and (b) the computational domain Ω. The inner most blue region shows the locations where the tumor cells will die out within 24 h. The outermost orange cells are predicted to die out within 72 h of exposure. Finally, the deep red cells towards the outside of the regions do not die after up to 72 h of exposure.

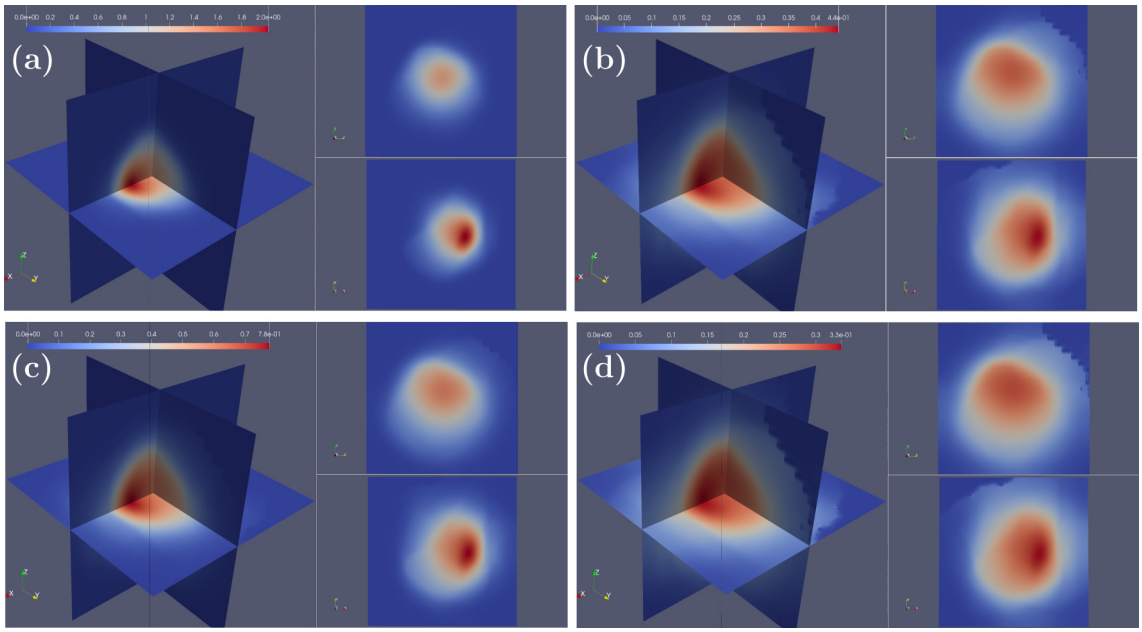

FIG. 6. Concentration profiles for an initial injection of $U_0 = 1.5\ \mu$M centered at $\mathbf{x}_c = (6.4\,\text{mm}, 0, 0)$ at $t = 0.2, 0.5, 0.8, 1$ in seconds, (a)–(d), respectively. The heat map is scaled to the visible range for each figure; i.e., the intensities are with respect to the concentration distribution in each figure independently of the other figures. Each figure is displayed with the intersection of three representative slices and two separate views of the frontal, yz plane, and transverse xy plane. The inhomogeneous- anisotropic nature of the diffusion can be observed in the planar slices accompanying the 3D figures.

In Fig. 5, we present the apoptotic region induced by the initial bump function within the tumor region $\mathbb{T}$ [Fig. 5(a)] and the entire computational domain Ω [Fig. 5(b)]; that is, the region of cells expected to die within an exposure time τ simply due to the initial condition before any diffusive spreading has occurred. In the figure, the outermost red region represents the location of the cells where the drug concentration is below any threshold value. The innermost dark blue region shows the locations where the concentration is above the threshold value $u_T(24)$, and the heat map illustrates regions where the concentration of the bump function is above the respective threshold values.

As the drug diffuses across the computational domain, Ω, more cells are exposed to the drug over the course of the simulation. Figure 6 shows the planar projections of the concentration profiles as a heat map at increasing simulation times. Red represents a higher concentration of drugs and deep blue represents a concentration of zero. To improve the visibility of simulations, we scale the data to visible data range. The inhomogeneous-anisotropic nature of the diffusion can be clearly observed from the concentration profiles in Fig. 6.

Now, we can compute the concentration levels at particular simulations times and compare them to the threshold values. For a particular simulation time, t_n, the volume fraction of the tumor where the concentration is above the threshold, $u_T(\tau)$, is calculated and summed with that of all previous times t_i where $i < n$, using Eq. (17). When this is done for the final time, $t_n = T$, which is chosen to be large enough that all of the drug mixture leaks away after this time, then we have our apoptosis fraction, $\aleph(\tau)$ in Eq. (18). We report the exact fractions, $\beth(\tau, t_n)$, from Eq. (17) in Table I. Note that the fourth column presents the final values that indicate the percentage of the tumor cells killed, $\aleph(\tau)$.

The effects of the inhomogeneous-anisotropic diffusion on apoptosis can be observed in Fig. 7. For example, the drug efficacy is significantly higher on the transverse plane compared to the sagital and frontal planes. This can be seen in Fig. 7(h) where the apoptotic region covers almost the entire transverse plane, while nontrivial portions of the frontal plane remains unscathed. Moreover, even though relatively high apoptosis fractions are achieved in the tumor region, $\mathbb{T}$, it is observed in Fig. 8 that significant amounts of the drug leak out of $\mathbb{T}$. So our results indicate that considerable portions of the healthy cells are subject to toxicity. We can visually inspect the leakage of the drug by superimposing the representative slices of the computational domain Ω and the subregion $\mathbb{T}$ (Fig. 8).

It is observed in Table I that the current configuration of the problem leads to partial ablation in the tumor region since 92% of the region dies after 72 h. In fact, as shown in the dose-response curves in Fig. 9, the apoptosis fraction seemingly asymptotes as we increase the amount of initial injection because the interaction of the drug with several obstacles, local inhomogeneities, and leakage, do not allow sufficient concentrations to diffuse to every part of the tumor region. Thus, we can conclude that our mechanistic model is

TABLE I. Convergence of apoptosis fraction approximation for $U_0 = 1.5\ \mu$M.

	$t_n = 0.2s$	$t_n = 0.5s$	$t_n = 0.8s$	$t_n = 1s$	$t_n = 1.2s$
$\beth(24, t_n)$	0.498408	0.528229	0.528229	0.528229	0.528229
$\beth(48, t_n)$	0.698709	0.814072	0.864979	0.873871	0.877210
$\beth(72, t_n)$	0.750721	0.878613	0.909647	0.915700	0.921299

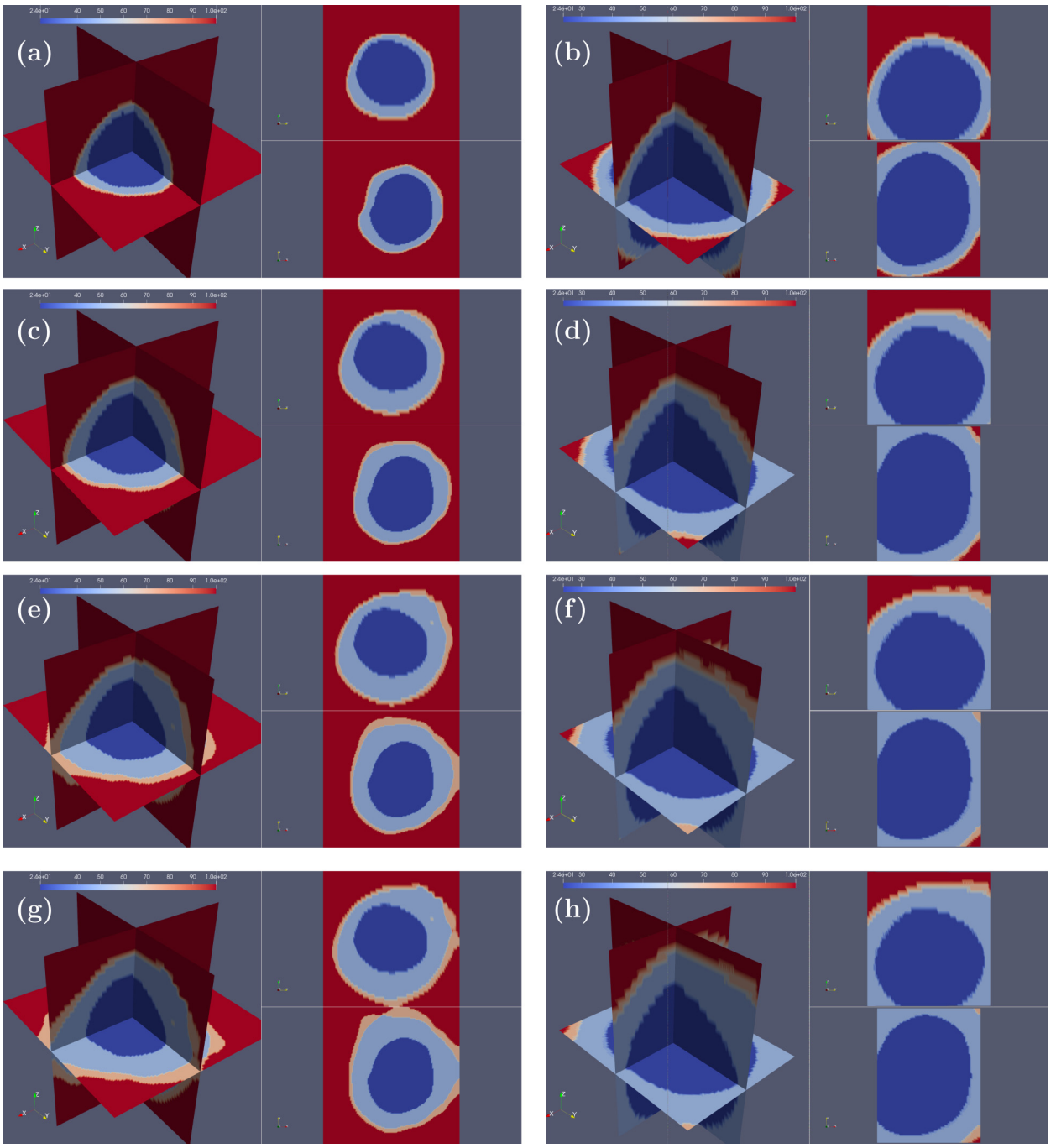

FIG. 7. Cells with a drug concentration higher than the given threshold, $\beth(\tau, t_n)$, at simulation times $t_n = 0.2,\ 0.5,\ 0.8,\ 1$, in seconds [(a),(b) to (g),(h)], respectively, after an initial injection of $U_0 = 1.5\ \mu$M centered at $\mathbf{x}_c = (6.4\,\text{mm}, 0, 0)$. The column on the left, (a), (c), (e), (g), shows the entire computational domain, Ω, and the column on the right, (b), (d), (f), (h), shows the tumor region, $\mathbb{T}$. Each figure is displayed with the intersection of three representative slices and two separate views of the frontal, yz plane, and transverse xy plane. It is observed that the number of cells exposed to a sufficient amount of drugs is higher on transverse, compared to the sagital, xz plane, and the frontal plane. The inner most blue region shows the locations where $u(\mathbf{x}, t) > u_T(\tau = 24\,\text{hours})$ for any $t = t_n$. The outermost orange cells correspond to $\tau = 72$ hours. Finally, the deep red cells towards the outside of the regions has concentrations $u(\mathbf{x}, t) < u_T(\tau)$ for all t and τ.

capable of reflecting the diffusion patterns mostly governed by location-wise structural differences.

Considering the internal injection scenario, several ways can be proposed to improve the efficacy of the drug without changing its fluidic properties. An obvious way may be to use a higher initial concentration, U_0. In fact, we can create dose-response curves for a broader view of the effects of various initial concentrations U_0 on the final apoptosis fractions. Figure 9 demonstrates the final percentages of the tumor that is killed for 31 different initial injections varying from $U_0 = 0.01\ \mu$M to $U_0 = 5\ \mu$M. Dose-response curves reveal that even though the initial injection is excessively elevated,

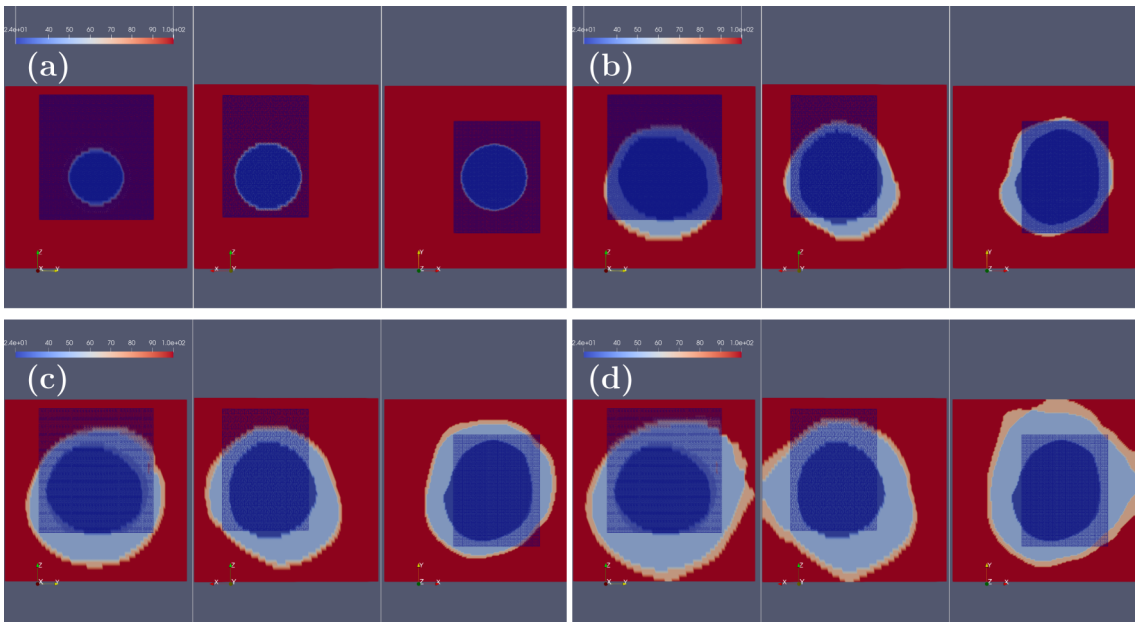

FIG. 8. A visual demonstration of toxicity. The effect of the threshold is extended beyond the tumor region, $\mathbb{T}$ (the dark blue rectangular mesh), and the heat map is calculated in the yz, xz, and xy planes from Eq. (17) at simulation times $t_n = 0,\ 0.2,\ 0.5,\ 1$, in seconds [(a)–(d)] respectively. It is observed that most of the drug mixture eventually diffuses outside of the tumor region. Thus, significant portions of healthy cells may potentially be subjected to toxicity. The inner most blue region shows the locations where $u(\mathbf{x}, t) > u_T(\tau = 24\,\text{hours})$ for any $t = t_n$. The outermost orange cells correspond to $\tau = 72$ h. Finally, the deep red cells towards the outside of the regions has concentrations $u(\mathbf{x}, t) < u_T(\tau)$ for all t and τ.

it is not possible to reach a complete tumor ablation. Indeed it is observed that apoptosis fractions barely improve after approximately $U_0 = 2\ \mu$M for $\tau = 48$ and 72 h exposure times. We reported in Fig. 8 that even $U_0 = 1.5\ \mu$M causes the presence of significant concentrations of drugs outside of the tumor region $\mathbb{T}$. Thus we can conclude that the use of initial drug concentrations outside of a certain range is prohibitive and can severely contribute to toxicity.

Another important parameter effecting the apotosis fraction is the location of injection. Our initial choice as the center of the bump function is (6.4 mm, 0, 0), which we pick by visual inspection to be near the center of the tumor. We found that changing the injection location greatly effects the diffusion pattern, and hence the final apoptosis fraction. In this sense, an important prediction in this investigation is that a seemingly poor location in $\mathbb{T}$ in terms of the distance from the center of the tumor bulk can yield higher apoptosis fractions than some locations that are close to the tumor center. To illustrate this phenomenon, in Fig. 10, we choose four different injections points $P_1(6.4, -3.84, -6.4)$, $P_2(-3.84, 0, -7.68)$, $P_3(-3.84, -3.84, -7.68)$, and $P_4(0, 12.8, 0)$ (all in mm), and create dose response curves for each location. Our results demonstrate that finding the optimal injection location to maximize apoptosis fractions is quite an unpredictable process and cannot be achieved with a basic visual inspection. For example, we pick P_4 to be the "poor" location considering its position relative to the center of the tumor, and expected to get lower apoptosis fractions compared to the other locations, but Fig. 10 shows a different outcome. Although P_1, P_2, and P_3 yield relatively similar patterns, P_4 produces a better results for 48 and 72 exposure times after $U_0 = 0.8\ \mu M$. However, efficacy is remarkably low for P_1 comparing to others if one opts to measure the apoptosis after 24 h. We should also note that similar to the initial findings, none of these configurations lead to full ablation in the tumor region.

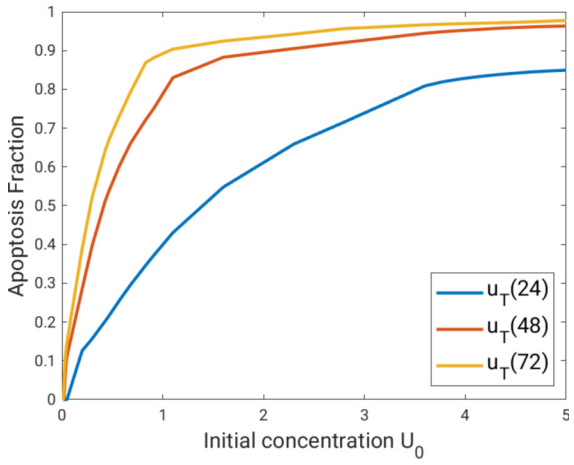

FIG. 9. Dose-response curves (24, 48, and 72 h from bottom to top) produced from 31 different initial injection concentrations varying from over the interval $[0.01, 5]$. It can be seen that the apoptosis fraction starts to asymptote beyond $U_0 = 2\ \mu M$ for 48 and 72 h exposure options.

We can further investigate this idea in a slightly different context. Let us manually choose 20 different injection points around the tumor region and calculate the apoptosis fractions by fixing the initial injection to $U_0 = 1.5\,\mu$M. We then label corresponding locations with these fractions and display them inside the tumor region $\mathbb{T}$ in Fig. 11. In the figure, blue points represent lower efficacy (69%) and red points represent higher

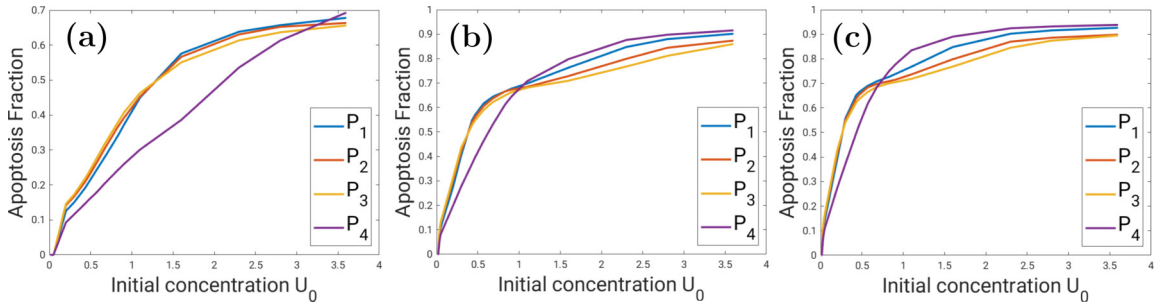

FIG. 10. Dose-response curves with four different injection points: $P_1(6.4, -3.84, -6.4)$, $P_2(-3.84, 0, -7.68)$, $P_3(-3.84, -3.84, -7.68)$, and $P_4(0, 12.8, 0)$ (all in mm). (a) 24 h dose-response curves. (b) 48 h dose-response curves. (c) 72 h dose-response curves. Although P_4 is picked as an intuitively "poor" location in terms of distance to the center of the tumor bulk, it yields better efficacy for 48 and 72 h exposure times after $U_0 = 1$ μM and $U_0 = 0.7$ μM, respectively.

efficacy (90%) for an exposure of 72 h. It is observed that the injection location has a significant influence on the efficacy of the drug. For example, in Fig. 11, $P_4(0, 1, 0)$ (the right most red point) from Fig. 10 is represented and had a much higher efficacy than several points taken around the center. In a realistic treatment case, one can increase the number of points used in the simulations to obtain broader information about the optimal injection sites. However, if the same figure is created with a sufficient number of injection points around (and even outside) the tumor region, we can create a more fine-grained apoptosis heat map. In this way, we can obtain a volumetric partition of the tissue of interest with respect to mean apoptosis fractions. Such a work-flow can allow practitioners to determine the optimal infusion locations. Once the corresponding partition is identified, we can utilize the simulation to find an ideal injection amount which can strike a balance between toxicity and efficacy.

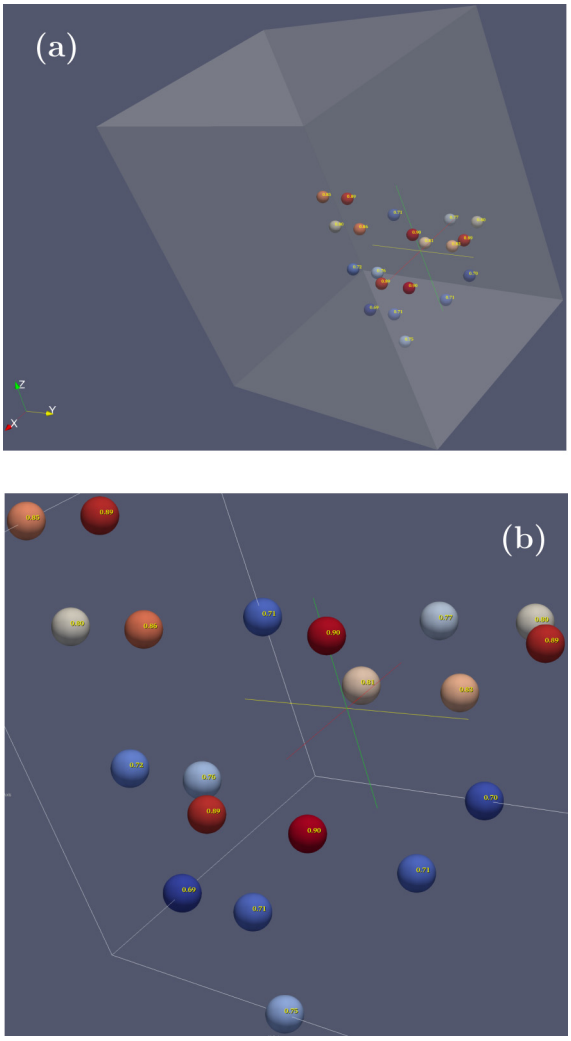

FIG. 11. Location based apoptosis fractions with $U_0 = 1.5$ μM based on 20 injection points. The numbers attached to the points are the predicted apoptosis fractions at these locations. (b) is a magnified version of (a).

In 3D simulations, computation time is undoubtedly of great importance and essentially determines if the proposed model is feasible in practical applications. In finite element models, the type and number of elements in the computational domain is the primary factor effecting the computation time. In this paper, we constructed the domain with 98403 bi-quadratic hexagonal elements. We should note that the number of elements must be determined by the number of diffusion tensors existing in the segmented volume of the original data.

Our computing environment is 9th Generation Intel(R) Core(TM) i7-9750H (12MB Cache, up to 4.5 GHz, 6 cores) with 32GB DDR4-2666MHz RAM. We run the simulations with an MPI-based parallel environment on four cores and observed that computation time is approximately 15 min for one simulation with an initial injection of $U_0 = 1.5$ μM and an output of apoptosis fractions for a given threshold, $u_T(\tau)$, the results of which are reported in Table I and 5.2 h to create the dose-response curve using 31 initial injection values in Fig. 9. We should carefully note that the number of elements in this framework should be completely determined by the dimension of the diffusion tensor volume extracted from the original data. Thus, to be able to describe the corresponding quantities in finer detail, diffusion tensor images with higher resolutions are needed, but in this case we need a more powerful environment to obtain the results in a reasonable computing time.

In future studies, a more realistic computational domain may be created. For simplicity, we worked with a cubic domain in this study. However, it may possible to locate and cut out the tumor region more accurately and create a volumetric

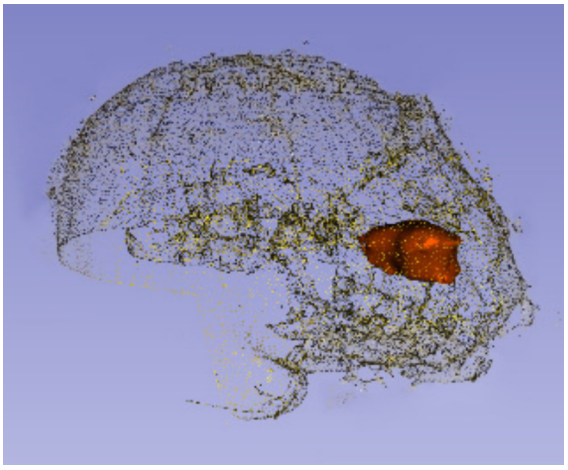

FIG. 12. Approximate tumor region segmented from the original DTI volume. The primary tumor region can be seen in red along with a discretized representation of the brain.

mesh based on this segmented region. A rough description of the tumor region extracted from the original data can be seen in red in Fig. 12. We display the tumor along with a discretized representation of the brain. We can then feed this mesh structure into the existing model. This approach has the potential to generate a more realistic model, but it can be quite challenging. For example, we would need to properly address how to interpolate the diffusion tensors across the boundary of this new domain if boundary conditions are to be imposed only on the surface of the tumor volume.

V. CONCLUSION AND FUTURE WORK

Brain tissue poses a unique transport challenge due to the highly inhomogeneous-anisotropic nature of the medium. Since drug exposure directly impacts cell death, the geometry and topography of the tumor will have a significant effect on efficacy. Further, the tumor will also grow in an inhomogeneous -anisotropic manner [45–48], and hence its structure can be quite unpredictable. DTI provides structure level information on an individual basis [49]. While there have been articles on employing DTI to study drug transport in the brain [5], thus far none have simulated the efficacy of a drug as a consequence of drug transport. With a drug transport- tumor population coupled model, there is potential for producing computer aided treatment strategies.

The response of cancer cells to a therapeutic agent is undoubtedly a highly complex phenomenon. However, some aspects of it can be addressed with the help of a mathematical model. In this sense, our aim in this study was to build a partial differential equation framework based on patient-specific data that can be used to predict the efficacy of drug diffusion in the brain tissue occupied by tumor cells. Moreover, this framework may be used to create diffusion models which take into account more complex considerations. For example, a problem encountered in some cancer therapies is drug resistance, which can be defined as the ability of cancer cells to survive and grow despite various anticancer treatments [72]. Further, oxygen concentration also has an effect on drug efficacy [73–76]. In this paper, we assumed that the tumor cells exposed to a drug concentration above certain threshold values will be ablated after the corresponding exposure times. Finally, our model does not accommodate gliomatosis cerebri where the infiltration is so extensive that no central focal area of the tumor can be located [77]. However, if reliable empirical knowledge is present about drug resistance, oxygen concentration, and a fine grained map of the infiltration, a time dependent or location-based threshold model may be integrated into this framework. In this regard, using finite element method in the model provides flexibility since it allows us to attach scalar quantities in the desired locations.

In future studies we propose to integrate this mechanistic model with a statistical model capable of predicting dose-response curves for new individuals for whom we have access to genetic information as well as DTI/MRI images of tumors. Our mechanistic pharmacokinetic models (PKM), in their original form, may not predict the drug response in new patients. Omics models, on the other hand, connects the genetic information of patients with their drug responses to predict the expected response for the same drug in a new patient. However, most Omics models do not explicitly take into account the properties of the tumor. Therefore, the Omics based model will produce similar expected response to the same drug among patients with similar genetic makeup even though their tumors may have very different diffusivities. Naturally, we would like to incorporate both pharmacokinetic and Omics based models to increase our understanding of the impact of tumor and genetic heterogeneity on drug responses. However, combining these two approaches are difficult because PKM cannot handle the high dimensional nature of genetic information (typically in the order of tens-of-thousands), while the Omics based models use a regression framework to connect drug response with genetic information and the physical properties of the tumor can be viewed as a predictor at best, thereby losing the spatial information of local diffusivities and tumor geometry.

The model we propose can offer a way combine PKM with Omics methodology in the following fashion. Observe that, the binary population model (Sec. II A) is the key construct that connects the concentration profile with the observed dose-response curves via three free time-invariant parameters a, b, and c. Now, if two patients with similar tumor properties produce different responses to the same drug, the foregoing free parameters will be able to capture the differences. Therefore, we view these parameters as individual-specific and any individual differences will be captured via these parameters. Consequently, a regression model connecting these parameters with Omics data can be posited. Once the regression model is trained, we can predict $\hat{a}$, $\hat{b}$, and $\hat{c}$ for a new patient and use these estimates with the PKM output to predict the dose response for new patient with different genetic information and tumor diffusivities.

It should be noted that this work assumes histological constancy (genetic homogeneity), however within a patient tumor this may not be the case [78–81]. Moreover, there may be temporal heterogeneity, which may lead to therapeutic resistance [78,82]. However, targeted therapy protocols often do not consider these heterogeneities and focus on the presence or absence of mutations despite the fact the

intratumor heterogeneity may induce different responses to the same therapeutic agent in different regions of the tumor thereby severely impacting expected outcome [82,83]. Several therapeutic strategies have been proposed to accommodate such heterogeneity [84,85]. Despite the histological constancy assumption, mathematically, multifoci drug delivery is more beneficial than single focus modes. Although this finding is yet to be experimentally tested in the context of GBM, we note that theranostic experiments conducted on heterogeneous ovarian cancer demonstrated multifoci delivery of nanoparticle drugs elicited a strong therapeutic response [86]. In fact, our approach offers mathematical support to therapeutic strategies that rely on noninvasive imaging to identify molecular subtypes in tumors to guide the course of treatment [87].

In addition, while the binary population model has computational advantages due to its simplicity, a more accurate model would be a stochastic dynamical system that is dependent on the concentration threshold. One concern may be the complexity of coupling, but fortunately transport happens on a much faster timescale than apoptosis. We would solve the partial differential equations for the transport, and then tackle the population dynamics to produce the apoptosis fractions. However, as with any model, adding more complexity is counterproductive unless it is accompanied by reliable data.

These challenges give the scientific community a singular opportunity to develop both biological and physical experiments to accurately estimate parameters and test the models.

ACKNOWLEDGMENTS

E.K. and E.A. are grateful to NSF (Grant No. DMS-1912902) for partial support of their contributions to this investigation. E.K., A.R., E.A., and S.G. appreciate the support of the Department of Mathematics and Statistics at TTU, S.G. also appreciates the support of the Department of Statistics at UNL, and A.R. appreciates the support of the Department of Applied Mathematics at UW. Finally, we would like to give our heartfelt thanks to the referees for their detailed suggestions, which played an integral part in improving this manuscript.

[1] Cancer.net, J. Oncol. Pract. **4**, 188 (2008).
[2] A. Parodi, M. Rudzińska, A. A. Deviatkin, S. M. Soond, A. V. Baldin, and A. A. Zamyatnin, Established and emerging strategies for drug delivery across the blood-brain barrier in brain cancer, Pharmaceutics **11**, 245 (2019).
[3] X. Wei, X. Chen, M. Ying, and W. Lu, Brain tumor-targeted drug delivery strategies, Acta Pharm. Sinica B **4**, 193 (2014).
[4] R. Daneman, The blood–brain barrier in health and disease, Ann. Neurol. **72**, 648 (2012).
[5] A. G. De Boer and P. J. Gaillard, Drug targeting to the brain, Annu. Rev. Pharmacol. Toxicol. **47**, 323 (2007).
[6] D. R. Groothuis, The blood-brain and blood-tumor barriers: A review of strategies for increasing drug delivery, Neuro-oncology **2**, 45 (2000).
[7] I. Choi, R. Strauss, M. Richter, C. Yun, and A. Lieber, Strategies to increase drug penetration in solid tumors, Front. Oncol. **3**, 193 (2013).
[8] V. G. Budker, S. D. Monahan, and V. M. Subbotin, Loco-regional cancer drug therapy: Present approaches and rapidly reversible hydrophobization (rrh) of therapeutic agents as the future direction, Drug Discov. Today **19**, 1855 (2014).
[9] R. Morhard, C. Nief, C. B. Castedo, F. Hu, M. Madonna, J. L. Mueller, M. W. Dewhirst, D. F. Katz, and N. Ramanujam, Development of enhanced ethanol ablation as an alternative to surgery in treatment of superficial solid tumors, Sci. Rep. **7**, 8750 (2017).
[10] I. Sagiv-Barfi, D. K. Czerwinski, S. Levy, I. S. Alam, A. T. Mayer, S. S. Gambhir, and R. Levy, Eradication of spontaneous malignancy by local immunotherapy, Sci. Transl. Med. **10**, eaan4488 (2018).
[11] R. K. Jain, Delivery of molecular and cellular medicine to solid tumors, Microcirculation **4**, 1 (1997).
[12] MunJu Kim, R. J. Gillies, and K. A. Rejniak, Current advances in mathematical modeling of anti-cancer drug penetration into tumor tissues, Front. Oncol. **3**, 278 (2013).
[13] Z. Wang, J. D. Butner, V. Cristini, and T. S. Deisboeck, Integrated pk-pd and agent-based modeling in oncology, J. Pharmacokinet. Pharmacodyn. **42**, 179 (2015).
[14] L. T. Curtis, V. H. van Berkel, and H. B. Frieboes, Pharmacokinetic/pharmacodynamic modeling of combination-chemotherapy for lung cancer, J. Theor. Biol. **448**, 38 (2018).
[15] C. L. Waite and C. M. Roth, Nanoscale drug delivery systems for enhanced drug penetration into solid tumors: Current progress and opportunities, Crit. Rev. Biomed. Eng. **40**, 21 (2012).
[16] M. Wu, H. B. Frieboes, M. A. J. Chaplain, S. R. McDougall, V. Cristini, and J. S. Lowengrub, The effect of interstitial pressure on therapeutic agent transport: coupling with the tumor blood and lymphatic vascular systems, J. Theor. Biol. **355**, 194 (2014).
[17] P. Dogra, J. D. Butner, Y.-li Chuang, S. Caserta, S. Goel, C. J. Brinker, V. Cristini, and Z. Wang, Mathematical modeling in cancer nanomedicine: a review, Biomed. Microdevices **21**, 40 (2019).
[18] William H Gmeiner and S. Ghosh, Nanotechnology for cancer treatment, Nanotechnology reviews **3**, 111 (2015).
[19] S. Tran, P.-J. DeGiovanni, B. Piel, and P. Rai, Cancer nanomedicine: A review of recent success in drug delivery, Clinical translational medicine **6**, 44 (2017).
[20] L. T. Curtis, M. Wu, J. Lowengrub, P. Decuzzi, and H. B. Frieboes, Computational modeling of tumor response to drug release from vasculature-bound nanoparticles, PloS ONE **10**, e0144888 (2015).
[21] A. L. Van D. Ven, M. Wu, J. Lowengrub, S. R. McDougall, M. A. J. Chaplain, V. Cristini, M. Ferrari, and H. B. Frieboes, Integrated intravital microscopy and mathematical modeling to optimize nanotherapeutics delivery to tumors, AIP Adv. **2**, 011208 (2012).
[22] L. T. Curtis, C. G. England, M. Wu, J. Lowengrub, and H. B. Frieboes, An interdisciplinary computational/experimental

approach to evaluate drug-loaded gold nanoparticle tumor cytotoxicity, Nucleic Acids Res. **11**, 197 (2016).

[23] P. Dogra, J. D. Butner, J. Ruiz Ramírez, Y.-li Chuang, A. Noureddine, C J. Brinker, V. Cristini, and Z. Wang, A mathematical model for nanomedicine pharmacokinetics and tumor delivery, Comput. Struct. Biotechnol. J. **18**, 518 (2020).

[24] K. H. Støverud, M. Darcis, R. Helmig, and S. M. Hassanizadeh, Modeling concentration distribution and deformation during convection-enhanced drug delivery into brain tissue, Transp. Porous Media **92**, 119 (2012).

[25] M. Sefidgar, M. Soltani, K. Raahemifar, M. Sadeghi, H. Bazmara, M. Bazargan, and M. M. Naeenina, Numerical modeling of drug delivery in a dynamic solid tumor microvasculature, Microvasc. Res. **99**, 43 (2015).

[26] M. Steuperaert, G. F. D'Urso Labate, C. Debbaut, O. De Wever, C. Vanhove, W. Ceelen, and P. Segers, Mathematical modeling of intraperitoneal drug delivery: simulation of drug distribution in a single tumor nodule, Drug Delivery **24**, 491 (2017).

[27] J. C. Panetta, A mathematical model of drug resistance: heterogeneous tumors, Math. Biosci. **147**, 41 (1998).

[28] J. M. Greene, C. Sanchez-Tapia, and E. D. Sontag, Mathematical details on a cancer resistance model, Front. Bioeng. Biotechnol. **8**, 501 (2020).

[29] Y. Watanabe, E. L. Dahlman, K. Z. Leder, and S. K. Hui, A mathematical model of tumor growth and its response to single irradiation, Theor. Biol. Med. Modell. **13**, 6 (2016).

[30] A. Yin, D. Jan A. R. Moes, J. G. C. van Hasselt, J. J. Swen, and H.-J. Guchelaar, A review of mathematical models for tumor dynamics and treatment resistance evolution of solid tumors, CPT: pharmacometrics systems pharmacology **8**, 720 (2019).

[31] A. M. Jarrett, A. Shah, M. J. Bloom, M. T. McKenna, D. A. Hormuth, T. E. Yankeelov, and A. G. Sorace, Experimentally-driven mathematical modeling to improve combination targeted and cytotoxic therapy for her2+ breast cancer, Sci. Rep. **9**, 1 (2019).

[32] H. P. Greenspan, Models for the growth of a solid tumor by diffusion, Stud. Appl. Math. **51**, 317 (1972).

[33] V. Andasari, A. Gerisch, G. Lolas, A. P. South, and M. A. J. Chaplain, Mathematical modeling of cancer cell invasion of tissue: biological insight from mathematical analysis and computational simulation, J. Math. Biol. **63**, 141 (2011).

[34] P. Macklin and J. Lowengrub, Nonlinear simulation of the effect of microenvironment on tumor growth, J. Theor. Biol. **245**, 677 (2007).

[35] P. Macklin, S. McDougall, A. R. A. Anderson, M. A. J. Chaplain, V. Cristini, and J. Lowengrub, Multiscale modeling and nonlinear simulation of vascular tumour growth, J. Math. Biol. **58**, 765 (2009).

[36] K. A. Rejniak and A. R. A. Anderson, Hybrid models of tumor growth, Wiley Interdiscp. Rev. Syst. **3**, 115 (2011).

[37] S. R. McDougall, A. R. A. Anderson, M. A. J. Chaplain, and J. A. Sherratt, Mathematical modeling of flow through vascular networks: implications for tumour-induced angiogenesis and chemotherapy strategies, Bull. Math. Biol. **64**, 673 (2002).

[38] M. A. Chaplain and A. R. Anderson, Mathematical modeling, simulation and prediction of tumour-induced angiogenesis, Invasion Metastasis **16**, 222 (1996).

[39] A. R. A. Anderson, M. A. J. Chaplain, E. L. Newman, R. J. C. Steele, and A. M. Thompson, Mathematical modeling of tumour invasion and metastasis, Comput. Math. Methods Med. **2**, 490902 (2000).

[40] K. Iwata, K. Kawasaki, and N. Shigesada, A dynamical model for the growth and size distribution of multiple metastatic tumors, J. Theor. Biol. **203**, 177 (2000).

[41] Y. Kuang, J. D. Nagy, and S. E. Eikenberry, *Introduction to Mathematical Oncology* (Taylor and Francis, London, 2016), Vol. 1.

[42] A. Rahman, S. Ghosh, and R. Pal, Modeling of drug diffusion in a solid tumor leading to tumor cell death, Phys. Rev. E **98**, 062408 (2018).

[43] See Supplemental Material at http://link.aps.org/supplemental/10.1103/PhysRevE.102.062425 for the LINCS database excell sheet.

[44] http://lincs.hms.harvard.edu/db/

[45] E. Konukoglu, O. Clatz, B. H. Menze, B. Stieltjes, M. A. Weber, E. Mandonnet, H. Delingette, and N. Ayache, Image guided personalization of reaction-diffusion type tumor growth models using modified anisotropic eikonal equations, IEEE Trans. Med. Imaging **29**, 77 (2010).

[46] B. H. Menze, K. V. Leemput, A. Honkela, E. Konukoglu, M. A. Weber, N. Ayache, and P. Golland, A generative approach for image-based modeling of tumor growth, Inf. Process Med. Imaging **22**, 735 (2011).

[47] M. C. Colombo, C. Giverso, E. Faggiano, C. Boffano, F. Acerbi, and P. Ciarletta, Towards the personalized treatment of glioblastoma: Integrating patient-specific clinical data in a continuous mechanical model, PLoS ONE **10**, e0132887 (2015).

[48] C. Engwer, M. Knappitsch, and C. Surulescu, A multiscale model for glioma spread including cell-tissue interactions and proliferation, Math. Biosci. Eng. **13**, 443 (2016).

[49] L. J. O'Donnell and C.-F. Westin, An introduction to diffusion tensor image analysis, Neurosurg. Clin. N. Am. **22**, 185 (2011).

[50] A. Roniotis, G. C. Manikis, V. Sakkalis, M. E. Zervakis, I. Karatzanis, and K. Marias, High-grade glioma diffusive modeling using statistical tissue information and diffusion tensors extracted from atlases, IEEE Trans. Inf. Technol. Biomed. **16**, 255 (2012).

[51] C. Mekkaoui, P. Metellus, W. J. Kostis, R. Martuzzi, F. R. Pereira, J.-P. Beregi, T. G. Reese, T. R. Constable, and M. P. Jackowski, Diffusion tensor imaging in patients with glioblastoma multiforme using the supertoroidal model, PLoS ONE **11**, e0146693 (2016).

[52] S. Angeli, K. E. Emblem, P. Due-Tonnessen, and T. Stylianopoulos, Towards patient-specific modeling of brain tumor growth and formation of secondary nodes guided by dti-mri, NeuroImage: Clinical **20**, 664 (2018).

[53] H. J. Scherer, The forms of growth in gliomas and their practical significance, Brain **63**, 1 (1940).

[54] I. Newton, Scala graduum caloris, Philos. Trans. **22**, 824 (1701).

[55] M. G. Larson and F. Bengzon, *The finite element method: Theory, implementation, and applications* (Springer Science & Business Media, Berlin, 2013), Vol. 10.

[56] R. H. Kraft, P. J. Mckee, A. M. Dagro, and S. T. Grafton, Combining the finite element method with structural connectome-based analysis for modeling neurotrauma: connectome neurotrauma mechanics, PLoS Comput. Biol. **8**, e1002619 (2012).

[57] E. Ramasamy, O. Avci, B. Dorow, S.-Y. Chong, L. Gizzi, G. Steidle, F. Schick, and O. Röhrle, An efficient modeling-simulation-analysis workflow to investigate stump-socket

interaction using patient-specific, three-dimensional, continuum-mechanical, finite element residual limb models, Front. Bioeng. Biotechnol. **6**, 126 (2018).

[58] O. Clatz, M. Sermesant, P.-Y. Bondiau, H. Delingette, S. K. Warfield, G. Malandain, and N. Ayache, Realistic simulation of the 3D growth of brain tumors in MR images coupling diffusion with biomechanical deformation, IEEE Trans. Med. Imaging **24**, 1334 (2005).

[59] G. Bornia, S. Bná, and E. Aulisa, Femus web page, 2017, https://github.com/FeMTTU/femus

[60] I. K. Koerte and M. Muehlmann, *Diffusion Tensor Imaging*, (Springer, Berlin, 2014).

[61] S. Pujol and R. Kikinis, 3D slicer neurosurgical planning tutorial, Available at https://spujol.github.io/NeurosurgicalPlanningTutorial/, [cited 2019 October 17].

[62] A. Y. Fedorov, R. R. Beichel, J. Kalpathy-Cramer, J. Finet, J.-C. Fillion-Robin, S. Pujol, C. Bauer, D. K. Jennings, F. Fennessy, M. Sonka, J. M. Buatti, S. R. Aylward, J. V. Miller, S. Pieper, and R. Kikinis, 3d slicer as an image computing platform for the quantitative imaging network, Magn. Reson. Imaging **9**, 1323 (2012).

[63] S. E. Maier, Y. Sun, and R. V. Mulkern, Diffusion imaging of brain tumors, NMR Biomed. **23**, 849 (2010).

[64] J. Malmivuo and R. Plonsey, *Bioelectromagnetism. Appendix A. Consistent System of Rectangular and Spherical Coordinates for Electrocardiology and Magnetocardiology* (Oxford University Press, Oxford, 1995).

[65] F. Casanova, P. R. Carney, and M. Sarntinoranont, Effect of needle insertion speed on tissue injury, stress, and backflow distribution for convection-enhanced delivery in the rat brain, PLoS ONE **9**, e94919 (2014).

[66] A. M. Mehta, A. M. Sonabend, and J. N. Bruce, Convection-enhanced delivery, Neurotherapeutics **14**, 358 (2017).

[67] D. W. Laske, R. J. Youle, and E. H. Oldfield, Tumor regression with regional distribution of the targeted toxin tf-crm107 in patients with malignant brain tumors, Nat. Med. **3**, 1362 (1997).

[68] J. Vorges, R. Reszka, A. Gossmann, C. Dittmar, R. Richter, G. Garlip, H. H. Coenen, V. Strum, K. Wienhard, W.-D. Heiss, and J. A. H, Imaging-guided convection-enhanced delivery and gene therapy of glioblastoma, Ann. Neurol. **54**, 479 (2003).

[69] Z. Lidar, Y. Mardor, T. Jonas, R. Pfeffer, M. Faibel, D. Nass, M. Hadani, and Z. Ram, Convection-enhanced delivery of paclitaxel for the treatment of recurrent malignant glioma: A phase i/ii clinical study, J. Neurosurg. **100**, 472 (2004).

[70] A. Carpentier, F. Laigle-Donadey, S. Zohar, L. Capelle, A. Behin, A. Tibi, N. Martin-Duverneuil, M. Sanson, L. Lacomblez, S. Tailibert, L. Puybasset, R. V. Effenterre, J.-Y. Delattre, and A. F. Carpentier, Phase 1 trial of a cpg oligodeoxynucleotide for patients with recurrent glioblastoma, Neuro. Oncol. **8**, 60 (2006).

[71] S. Kunwar, S. M. Chang, M. D. Prados, M. S. Berger, J. H. Sampson, D. Croteau, J. W. Sherman, A. Y. Grahn, V. S. Shu, J. L. Dul, S. R. Husain, B. H. Joshi, C. Pedain, and R. K. Puri, Safety of intraparenchymal convection-enhanced delivery of cintredekin besudotox in early-phase studies, Neurosurg. Focus **20**, E15 (2006).

[72] M. Leary, S. Heerboth, K. Lapinska, and S. Sarkar, Sensitization of drug resistant cancer cells: a matter of combination therapy, Cancers **10**, 483 (2018).

[73] D. Pappas, in *Encyclopedia of Analytical Chemistry*, Single-cell Hypoxia: Current Analytical Techniques and Future Opportunities (Wiley, New York, 2016).

[74] T. Germain, M. Ansari, and D. Pappas, Observation of reversible, rapid changes in drug susceptibility of hypoxic tumor cells in a microfluidic device, Anal. Chim. Acta **936**, 179 (2016).

[75] G. Khanal, S. Hiemstra, and D. Pappas, Probing hypoxia-induced staurosporine resistance in prostate cancer cells with a microfluidic culture system, Analyst **139**, 3274 (2014).

[76] D. Iyer, R. D. Ray, and D. Pappas, High temporal resolution fluorescence measurements of a mitochondrial dye for detection of early stage apoptosis, Analyst **138**, 4892 (2013).

[77] E. C. Holland, Glioblastoma multiforme: The terminator, Proc. Natl. Acad. Sci. **97**, 6242 (2000).

[78] F. Michor and K. Polyak, The origins and implications of intratumor heterogeneity, Cancer Prev. Res. **3**, 1361 (2010).

[79] L. G. Martelotto, C. K. Ng, S. Piscuoglio, B. Weigelt, and J. S. Reis-Filho, Breast cancer intra-tumor heterogeneity, Breast Cancer Res. **16**, 210 (2014).

[80] N. Andor, T. A. Graham, M. Jansen, L. C. Xia, C. A. Aktipis, C. Petritsch, H. P. Ji, and C. C. Maley, Pan-cancer analysis of the extent and consequences of intratumor heterogeneity, Nat. Med. **22**, 105 (2016).

[81] A. Sottoriva, I. Spiteri, S. G. Piccirillo, A. Touloumis, V. P. Collins, J. C. Marioni, C. Curtis, C. Watts, and S. Tavaré, Intratumor heterogeneity in human glioblastoma reflects cancer evolutionary dynamics, Proc. Natl. Acad. Sci. USA **110**, 4009 (2013).

[82] N. McGranahan and C. Swanton, Biological and therapeutic impact of intratumor heterogeneity in cancer evolution, Cancer Cell **27**, 15 (2015).

[83] D. J. VanderWeele, R. Finney, K. Katayama, M. Gillard, G. Paner, S. Imoto, R. Yamaguchi, D. Wheeler, J. Lack, M. Cam, A. Pontier, Y. T. M. Nguyen, K. Maejima, A. Sasaki-Oku, K. Nakano, H. Tanaka, D. V. Griend, M. Kubo, M. J. Ratain, S. Miyano, and H. Nakagawa, Genomic heterogeneity within individual prostate cancer foci impacts predictive biomarkers of targeted therapy, Eur. Urol. Focus **5**, 416 (2019).

[84] R. A. Gatenby, A. S. Silva, Robert J. Gillies, and B. R. Frieden, Adaptive therapy, Cancer Res. **69**, 4894 (2009).

[85] N. Chatterjee and T. G. Bivona, Polytherapy and targeted cancer drug resistance polytherapy and targeted cancer drug resistance, Trends Cancer, **5**, 170 (2019).

[86] M. Satpathy, L. Wang, R. J. Zielinski, W. Qian, Y. A. Wang, A. M. Mohs, B. A. Kairdolf, X. Ji, J. Capala, M. Lipowska, S. Nie, H. Mao, and L. Yang, Targeted drug delivery and image-guided therapy of heterogeneous ovarian cancer using her2-targeted theranostic nanoparticles, Theranostics **9**, 778 (2019).

[87] N. Braman, P. Prasanna, J. Whitney, S. Singh, N. Beig, M. Etesami, D. D. B. Bates, K. Gallagher, B. N. Bloch, M. Vulchi, P. Turk, K. Bera, J. Abraham, W. M. Sikov, G. Somlo, L. N. Harris, H. Gilmore, D. Plecha, V. Varadan, and A. Madabhushi, Association of peritumoral radiomics with tumor biology and pathologic response to preoperative targeted therapy for her2 (erbb2)-positive breast cancer, JAMA Netw. Open **2**, e192561 (2019).